



H3K9 trimethylation dictates neuronal ferroptosis through repressing *Tfr1*

Ting Lan^{1,*}, Liye Hu^{1,*}, Tingting Sun¹, Xuechun Wang², Zhongnan Xiao¹, Danmin Shen¹, Weihua Wu¹, Zhaoli Luo¹, Chao Wei³, Xiaotong Wang³, Meng Liu³, Yi Guo², Liyong Wang⁴, Yamei Wang¹ , Yabin Lu¹, Yan Yu^{5,6,7}, Fei Yang^{3,8}, Chenguang Zhang^{1,9} and Qian Li^{1,8,9}

Abstract

Spontaneous intracerebral hemorrhage (ICH) is a devastating disease with high morbidity and mortality worldwide. We have previously shown that ferroptosis contributes to neuronal loss in ICH mice. The overload of iron and dysfunction of glutathione peroxidase 4 (GPx4) promote neuronal ferroptosis post-ICH. However, how epigenetic regulatory mechanisms affect the ferroptotic neurons in ICH remains unclear. In the current study, hemin was used to induce ferroptosis in N2A and SK-N-SH neuronal cells to mimic ICH. The results showed that hemin-induced ferroptosis was accompanied by an increment of global level of trimethylation in histone 3 lysine 9 (H3K9me3) and its methyltransferase Suv39h1. Transcriptional target analyses indicated that H3K9me3 was enriched at the promoter region and gene body of transferrin receptor gene 1 (*Tfr1*) and repressed its expression upon hemin stimulation. Inhibition of H3K9me3 with inhibitor or siRNA against Suv39h1 aggravated hemin- and RSL3-induced ferroptosis by upregulating *Tfr1* expression. Furthermore, Suv39h1-H3K9me3 mediated repression of *Tfr1* contributes to the progression of ICH in mice. These data suggest a protective role of H3K9me3 in ferroptosis post ICH. The knowledge gained from this study will improve the understanding of epigenetic regulation in neuronal ferroptosis and shed light on future clinical research after ICH.

Keywords

Intracerebral hemorrhage, neurons, ferroptosis, epigenetics, transferrin receptor

Received 18 February 2022; Revised 22 January 2023; Accepted 28 February 2023

Introduction

Spontaneous intracerebral hemorrhage (ICH) accounts for only 10–15% in all stroke subtypes, but holds the highest mortality.¹ ICH affects more than 1 million people each year worldwide, and most survivors suffer from severe sequelae due to a lack of effective therapeutic options.^{1,2} Hematoma formation and expansion lead to intracranial pressure elevation that

⁵Chinese Institute of Rehabilitation Science, China Rehabilitation Science Institute, Beijing, China

⁶Beijing Key Laboratory of Neural Injury and Rehabilitation, China Rehabilitation Research Center, Beijing, China

⁷School of Rehabilitation Medicine, Capital Medical University, Beijing, China

⁸Advanced Innovation Center for Human Brain Protection, Beijing Key Laboratory of Neural Regeneration and Repair, Capital Medical University, Beijing, China

⁹Beijing Key Laboratory of Cancer Invasion and Metastasis Research, Capital Medical University, Beijing, China

*These authors contributed equally to this work.

Corresponding authors:

Qian Li, Capital Medical University, Beijing 100069, China.
 Email: qianli@ccmu.edu.cn

Chenguang Zhang, Capital Medical University, Beijing 100069, China.
 Email: chzhang@ccmu.edu.cn

¹Department of Biochemistry and Molecular Biology, School of Basic Medical Sciences, Capital Medical University, Beijing, China

²School of Basic Medical Sciences, Capital Medical University, Beijing, China

³Department of Neurobiology, School of Basic Medical Sciences, Capital Medical University, Beijing, China

⁴Core Facilities for Molecular Biology, Capital Medical University, Beijing, China

causes brain damage and neuronal death. Subsequently, toxins, such as hemoglobin (Hb), heme, and iron, released from the red blood cells further contribute to neuronal death. Extracellular iron is transported into neurons mainly through the transferrin (TF)-TF receptor 1 (TFR1, the protein encoded by *Tfr1* gene) system.³ Overloaded free iron in the neuron can react with hydrogen peroxide (H₂O₂) to form more toxic hydroxyl radicals (\cdot OH) via the Fenton reaction, which causes damages to DNA, proteins, or lipids, and may induce several forms of cell death, including apoptosis, necroptosis, autophagy, and newly identified ferroptosis.^{4–6}

Ferroptosis, a non-apoptotic and regulated type of cell death, is caused by severe lipid peroxidation-mediated membrane damage in an iron-dependent manner.^{7,8} Factors that affect the metabolism of iron and/or lipids, as well as those that affect the redox systems are potential regulators of ferroptotic cell death. Erastin (the cysteine/glutamate antiporter inhibitor), RSL3 (inhibitor of glutathione peroxidase 4, GPx4), iron, and hemin (to increase intracellular iron and decrease GPx4 activity) are widely used to induce ferroptosis,^{7,9–11} whereas iron chelator deferoxamine (DFO) and lipid reactive oxygen species (ROS) scavenger ferrostatin-1 (Fer-1) are ferroptosis inhibitors.⁷ We and others have demonstrated that ferroptosis occurs during ICH and contributes to neuronal death *in vitro* and *in vivo*.^{5,11} More importantly, rescuing neuronal death, including ferroptosis, reduces brain injury, and improves functional outcomes of ICH animals effectively. Inhibiting ferroptosis thus represents a new target for the treatment of ICH.¹² However, administration of DFO didn't obtain optimistic results from clinical trials, and for Fer-1, as a small molecule compound, there is still a long way to go before clinical applications. Further investigation into the molecular mechanism of ferroptosis may give rise to new therapeutic options for treating ICH.

Epigenetic modification of DNA and histones at specific loci on chromatin plays fundamental roles in the regulation of gene expression and related biological processes. The post-translational modification of histones is extremely complicated that involves methylation, acetylation, ubiquitination, *etc.* The combination of different types of modification at specific histone residues constitutes the "histone code" to dictate gene expression.¹³ Among those, histone 3 lysine 9 trimethylation (H3K9me3) is a well-studied and conserved epigenetic modification. Its enrichment promotes constitutive heterochromatin formation and gene repression.^{14,15} The suppressor of variegation 3–9 homolog 1 and 2 (*Suv39h1/2*) and SET domain bifurcated histone lysine methyltransferase 1 (*SETDB1/ESET*) are methyltransferases of H3K9me3, while jumonji D2/lysine-specific demethylase 4A (*JMJD2/KDM4*) family members are the

corresponding demethylases.^{16–20} H3K9me3 has been shown to participate in a broad range of biological processes, including cell differentiation, embryonic development, cellular senescence, and malignancies.^{21–24} However, whether epigenetic regulation, especially H3K9me3, participates in neuronal ferroptosis during ICH is unknown.

In this study, we describe a novel role of H3K9me3 in neuronal ferroptosis. The level of H3K9me3 was increased in neuronal N2A cells after hemin treatment. H3K9me3 enriched at the promoter of the *Tfr1* gene and repressed its expression. Decreasing H3K9me3 levels by repressing the activity or depleting the expression of its methyltransferase *Suv39h1*, or knocking down *Tfr1* all effectively rescued neuronal ferroptosis induced by hemin and RSL3. Suppression of *Suv39h1* and up-regulation of *Tfr1* aggravates ICH in mice. Together, these findings will advance the understanding of neuronal ferroptosis following ICH and help to improve functional recovery using epigenetic strategies after stroke.

Material and methods

Animals

All male C57BL/6J (6–8 weeks) mice were obtained from Charles River Laboratories. Mice were housed at 20–26°C, 40–70% humidity and kept on a 12h light/dark cycle. Food and water were available ad libitum. Animal experiments were performed according to National Institutes of Health Guide and reported in compliance with ARRIVE guidelines (Animals in Research: Reporting *In vivo* Experiments). All animal experimental protocols were approved by the Institutional Animal Care and Use Committee of Capital Medical University.

Intracerebroventricular (i.c.v.) injection of siRNA

A mixture of three different siRNAs (200 μ M, Science artis, China) against *Suv39h1* or the scramble control siRNA were delivered 48 h before ICH modeling. The mice were anesthetized using 1–2% isoflurane (R510-22, RWD, China) inhalation and fixed on a stereotaxic frame (E04545, RWD). Then, a burr hole was drilled in the left skull and 0.5 μ L siRNA was injected at a rate of 0.1 μ L/min at the following coordinates relative to bregma: 0.5 mm anterior, 0.9 mm left lateral and 2.5 mm in the depth. The needle was held for 10 min after the injection. The craniotomy was sealed with Super Glue (1469SB, 3 M, USA). The sequences of the siRNAs are listed in Supplementary table 3.

Mouse ICH model

The mouse ICH model was established as previously described.²⁵ In brief, mice were anesthetized using 1–2% isoflurane inhalation and fixed on a stereotactic frame. A 0.6 mm burr hole was drilled in the left skull and 0.5 μ L collagenase (C2399, Sigma-Aldrich, USA) was injected at a rate of 0.1 μ L/min at the following coordinates relative to bregma: 0.8 mm anterior and 2.0 mm left lateral and 3.15 mm in the depth. The needle was held for 10 min after the injection and then the craniotomy was sealed with Super Glue (1469SB, 3M). Sham control mice received only needle insertion. Animal body temperature was maintained at 37°C throughout with a heating blanket.

Neurologic function assessment

Behaviors of the mice were tested at 12 h post ICH as previously reported.²⁵ Neurologic deficit scores included six parts, body symmetry, gait, climbing, circling behavior, front limb symmetry, and compulsory circling. Each test was graded from 0 to 4, and 4 indicates the most severe impairment. Forelimb placing test was used to assess the forelimb movements evoked by vibrissae-touching. The mice were placed on the edge of the table and brushed the vibrissae. Normal animals quickly placed their forelimbs on the table. The result was the probability of success for ten rounds of the trial. For hindlimb placing test, the mice were placed on the edge of the table and contralateral hind limb were pulled down. Behaviors were divided into three categories: immediate pullback (0 point), delayed pullback (1 point), inability to pull back (2 points). The results were the sum of the scores from 10 rounds of trials.

MDA measurement

Amount of MDA was measured by using MDA Assay kit (ab118970, Abcam) according to the manufacturer's instructions. Briefly, 10 mg ipsilateral striatum was collected and reacted with thiobarbituric acid (TBA) to generate an MDA-TBA adduct. The reaction mix was transferred to wells of microplate. The absorbance was measured immediately on a microplate reader (SpectraMax iD5, Molecular devices, USA) at OD 532 nm for colorimetric assay.

Cell cultures

The N2A and SK-N-SH cells were cultured in Dulbecco's modified eagle medium (DMEM) of high glucose (C11995500BT, Gibco, USA) containing 10% fetal bovine serum (FBS, 10099141, Gibco) and 1% penicillin-streptomycin mixture (KGY0023, Keygen,

China) at 37°C, 5% CO₂, 95% saturated humidity in an incubator. Cells were passaged every 3 days.

Drug administration

Unless specifically indicated, N2A and SK-N-SH cells were exposed to 15 μ M hemin (16009-13-5, Frontier Scientific, USA), 5 μ M RSL3 (S8155, Selleck, USA), Erastin (S7242, Selleck) 2 μ M Fer-1 (S7243, Selleck), 15 μ M DFO (D9533, Sigma-Aldrich), or 0.5 μ M Chaetocin (S8068, Selleck) for 24 hours.

MTT assay

N2A or SK-N-SH cells (1×10^4) were seeded in 96-well plates and maintained for 24 h (cell density reaches 70–80%). After treatment with different reagents, the medium was removed, and the cells were washed twice with PBS. Cells were incubated with 20 μ L of 5 mg/mL MTT solution (0793, Amresco, USA) for 4 hours. One hundred microliter DMSO (D8418, Sigma-Aldrich) was added to cells after removing MTT and incubated at 37°C for 10 min. Finally, absorbance at the wavelength of 570 nm was recorded with a microplate reader (SpectraMax iD5, Molecular DEVICES, USA).

Propidium iodide (PI) staining

N2A cells (2×10^4) were seeded in 48-well plates and cultured for 24 h until the cell density reaches 70–80%. After treating with the drugs, the cells were incubated with 1 μ L of 20 μ g/mL PI dye (P4170, Sigma-Aldrich) followed with observation under a fluorescence microscope (ECLIPSE CI, NIKON, Japan) and the percentage of PI⁺ cells were counted blindly.

Chromatin immunoprecipitation (ChIP)

N2A cells (1×10^7) were plated in 15 cm cell culture dishes and cultured for 24 h. Cells were treated with 15 μ M hemin or vehicle (0.075% DMSO) for 12 h. After removing the medium, the cells were incubated with 1% formaldehyde solution (F8775, Sigma-Aldrich) at 37°C for 10 min, followed by ultrasonic lysis and incubation with H3K9me3 (ab8898, Abcam, USA) or IgG (C1755, Applygen, China) antibodies at 4°C overnight. The antibody-protein-DNA complex was immunoprecipitated with protein A/G (sc-2003, Santa Cruz), and sequentially washed and eluted. After de-crosslinking at 65°C, the DNA was extracted and purified using a PCR Purification Kit (28106, QIAquick, Germany).

The primer sequences for the mouse *Tfr1* promoter and gene body used in the ChIP experiment are listed in Supplementary table 6.

ChIP-sequencing (ChIP-seq)

The chromatin DNA was immunoprecipitated with anti-H3K9me3 or IgG from N2A cells, followed with purification as mentioned above and the DNA sequencing was performed by Beijing igeneCode Biotech (Beijing, China) on the MGISEQ T7 platform. ChIP-seq reads were aligned to the mouse reference genome (GRCm38/mm10) using Soap2.21 (BGI, China) with parameters as: $-p\ 4\ -v\ 2\ -s\ 35$ and only the alignments within 2 mismatches were considered in peak calling, for which MACS2 (version 1.4.2) was employed with parameters as: $-bw\ 200\ -p\ 0.005\ -w\ -single-profile\ -space\ 50$. The genomic distribution of H3K9me3 was analyzed by ChIPseeker, an R package for peak annotation and comparison, while ClusterProfiler was employed for gene ontology (GO) analyses. Integrative Genomics Viewer (IGV) was used for peak visualization at the specific genomic locus. The ChIP-seq data have been deposited in GEO repository under accession number of GSE217972.

Lipid Reactive Oxygen Species (ROS) determination

N2A cells (2×10^4) were seeded in 48-well plates and treated with different drugs for 24 h. The cells were incubated with a lipid peroxidation sensor BODIPY C11 (D3861, Invitrogen, USA) for 30 min according to the manufacturer's instructions. After the medium was removed, the cells were washed three times with PBS. Fluorescence of different wavelengths was observed under a fluorescence microscope (ECLIPSE CI, NIKON, Japan), and the ratio of the fluorescence intensity emitted at 590 nm and 510 nm was calculated as the level of lipid ROS of the cells.

siRNA transfection *in vitro*

N2A cells cultured for 12–24 h were transfected with siRNAs when the cell density reached 30–50%. In brief, 10 μ L LipofectamineTM RNAiMAX (13778150, Invitrogen) was added into 1000 μ L Opti-MEMTM I reduced serum culture (31985070, Gibco), which were then mixed and incubated at room temperature for 5 min. Meanwhile, another mixture of 10 μ L siRNA (storage concentration was 20 μ M) with 1000 μ L Opti-MEMTM I reduced serum medium was prepared, which was then further mixed with the Opti-MEMTM containing the LipofectamineTM RNAiMAX and incubated at room temperature for 15–20 min. The medium in the culture plate was discarded, and the cells were washed twice with PBS solution. Two milliliters of the mixed solution mentioned above was added to each well, maintained in the cell incubator. Six hours later, the

transfection reagents were replaced with normal high glucose DMEM medium containing 10% FBS, 1% penicillin-streptomycin, and the cells were cultured for 48 h. The sequences of siRNAs are listed in Supplementary table 4.

Iron measurement

Ferrous and total iron were measured with Iron Assay kit (K390-100, Biovision, USA). N2A cells were dissociated by trypsinization. The cell suspension was collected and centrifuged. 100 μ L Iron Assay Buffer was added into the cell pellet. The samples were divided into two parts, 5 μ L Assay Buffer was added to 50 μ L samples for ferrous iron assay, and 5 μ L Iron Reducer was added to 50 μ L samples for total iron assay. The Iron Probe was then added, mixed and incubated for 60 min at 37°C. The output was measured immediately on a colorimetric microplate reader (SpectraMax iD5, Molecular devices) at OD 593 nm.

Statistical analysis

Data of experiments *in vitro* were presented in triplicate, and all statistical analyses were performed with GraphPad Prism 7.0. Before analyses, Shapiro-Wilk normality test was used to assess data distribution. When the data exhibit a normal distribution, two tailed Student's t test was used for comparison of two groups while one or two-way ANOVA followed by Tukey's multiple comparisons tests were performed for comparisons of multiple groups. Otherwise, non-parametric Kruskal-Wallis test followed by Dunn's multiple comparisons was employed for comparisons of multiple groups. Specific methods were indicated in figure legend. A *P* value less than 0.05 was considered to be statistically significant.

Results

Hemin induces ferroptosis in neuronal cells

In order to explore the epigenetic regulation of neuronal death after ICH, we used hemin to induce cell death in N2A neuronal cells.²⁵ Hemin markedly decreased the cell viability in both dose- and time-dependent manners (Figure 1(a) and (b)). The LD₅₀ of hemin was estimated as 15 μ M and this dosage was used for the rest of the experiments. Meanwhile, a human neuronal cell line SK-N-SH was also examined, and hemin also decreased its viability in dose- and time-dependent manners (Figure 1(c) and (d)).

To further identify if the cell death caused by hemin was ferroptosis,¹¹ cell death was assessed with

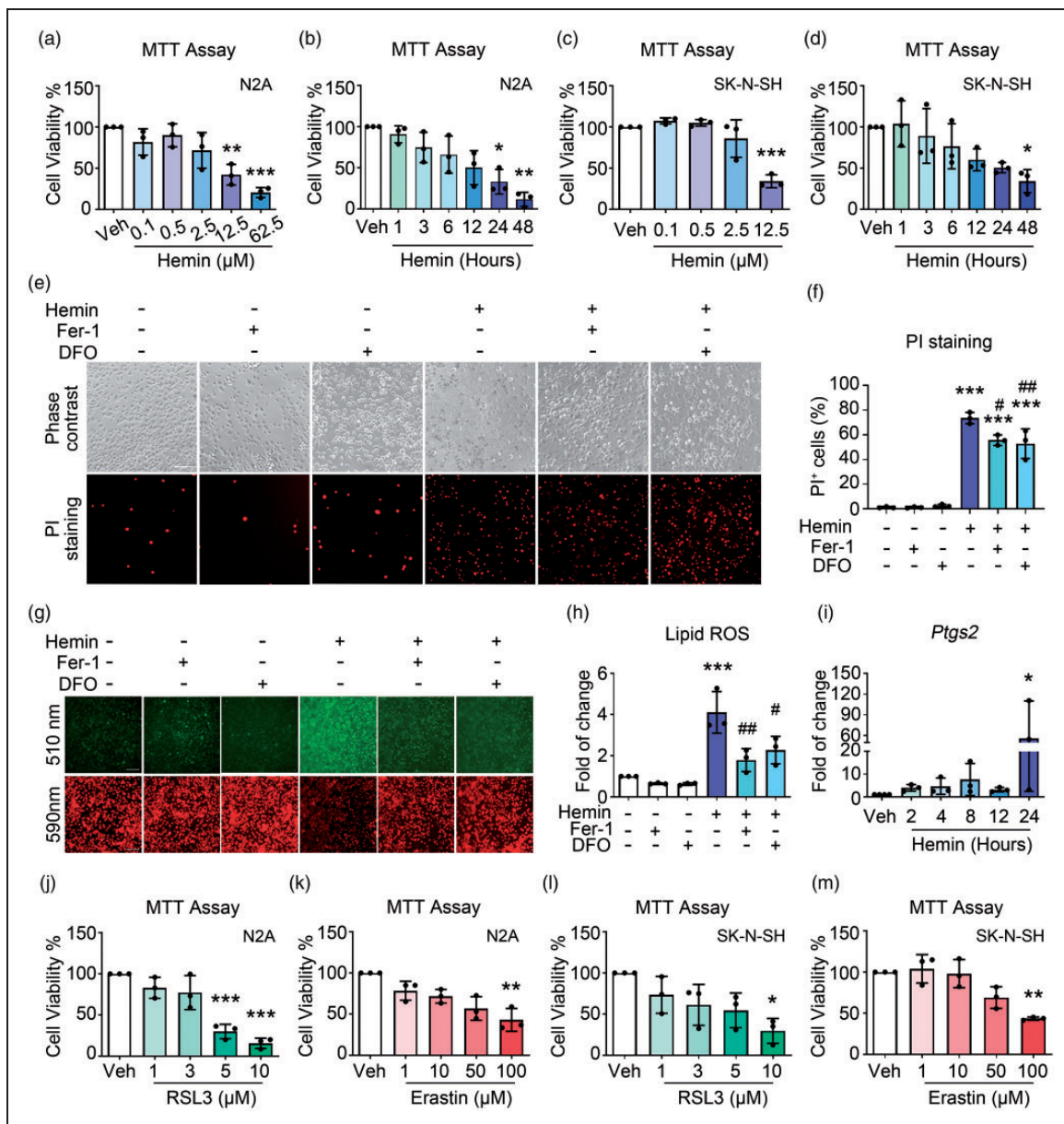


Figure 1. Hemin induces ferroptosis in neuronal cells. (a) N2A cells were incubated with hemin or vehicle, and cell viability was analyzed using MTT assays. (b) N2A cells were treated with 15 μM hemin or vehicle, and MTT assays were performed. (c) SK-N-SH cells were treated with different concentrations of hemin, and MTT assays were performed. (d) SK-N-SH cells were treated with 8 μM hemin for different time points, and MTT assays were performed. (e, f) N2A cells were treated as indicated, and PI staining was performed to detect cell death. Representative images (e) and quantifications (f) are shown. (g, h) N2A cells were treated as indicated, and BODIPY 581/591 C11 reagent was used for lipid ROS detection. Representative images (g) and quantifications (h) are shown. (i) N2A cells were treated with hemin or vehicle as indicated, and the mRNA expression of *Ptg2s* was detected using RT-qPCR. *GAPDH* serves as an internal control. (j, k) N2A cells were treated with RSL3 (j), Erastin (k), or vehicle as indicated, and MTT assays were performed. (l, m) SK-N-SH cells were treated with RSL3 (l), Erastin (m), or vehicle as indicated, and MTT assays were performed. Results are shown as scatter plots (Mean \pm SD). $n = 3$ independent experiments. One-way ANOVA (a, c, d, f, h, i, j, m) or Kruskal-Wallis test (b, k, l) followed by Tukey's or Dunn's multiple comparisons tests, respectively, were used. * $p < 0.05$, ** $p < 0.01$, *** $p < 0.001$ vs vehicle; # $p < 0.05$, ### $p < 0.01$ vs Hemin. Scale bar: (e, g) 100 μm .

PI staining. Hemin significantly increased the percentage of PI⁺ cells, and co-treatment with ferroptosis inhibitors, Fer-1 and DFO, effectively attenuated cell death induced by hemin (Figure 1(e) and (f)), indicating

that ferroptosis accounted for part of hemin-induced cell death in N2A cells. The accumulation of lipid reactive oxygen species (ROS) is a hallmark of ferroptosis. By staining with the BODIPY 581/591 C11 fluorescent

probes, hemin increased the level of lipid ROS, which was significantly reduced by Fer-1 and DFO (Figure 1 (g) and (h)). Hemin also greatly augmented the mRNA level of *Ptgs2* time-dependently (Figure 1(i)), another hallmark of ferroptosis. Furthermore, other ferroptosis inducers, RSL3 and Erastin, both induced ferroptosis in N2A cells (Figure 1(j) and (k)) and SK-N-SH cells (Figure 1(l) and (m)) in a dose-dependent manner as hemin did, suggesting that ferroptosis contributed to N2A cell death under hemin treatment.

Suv39h1-mediated H3K9me3 is increased and protects against hemin-induced ferroptosis

To investigate whether epigenetic regulation was involved in hemin-induced neuronal ferroptosis, N2A cells were treated with hemin and the levels of various well-characterized epigenetic modifications on histone residues were assessed. Compared with vehicle groups, the global level of transcriptional repression marker H3K9me3 was increased in a time-dependent manner, which reached a peak at 8 h and persisted till 24 h post hemin treatment (Figure 2(a) and (b)). The levels of other transcriptional repression markers, including H3K9me2, H3K9me1, H3K27me3, and H3K27me2 were not notably changed upon hemin treatment (Figure 2(a), (c) to (g)). The protein level of histone deacetylase 1 (HDAC1), the enzyme that deacetylates histone acetylation and mediates gene repression, also did not change markedly (Figure 2(e) and (h)). As gene repression and activation are dynamically and synergistically regulated, we additionally examined the level of markers for gene transcriptional activation, such as H3K4me2 and H3Kac, which did not show significant alterations either (Figure 2(i) to (l)).

To figure out the mechanism(s) underlying the increment of H3K9me3 upon hemin treatment, the mRNA levels of its methyltransferases (*Suv39h1*, *Suv39h2*, and *Setdb1*) and demethylases (*Kdm4a*, *Kdm4b*, *Kdm4c*, and *Kdm4d*) were detected in hemin-treated N2A cells. Compared with the vehicle group, the mRNA level of *Suv39h1* increased significantly as early as 2 h of hemin treatment (Figure 2(m)), while the levels of other enzymes did not change significantly at early stage of treatment (Figure 2(m) and (n)). The protein level of Suv39h1 showed mild increase since 2 h (though without significance), and reached peak at 12 h after hemin treatment (Figure 2(o)). Therefore, upregulation of *Suv39h1* responding to hemin treatment might contribute to the increase of H3K9me3 levels during the later time points of hemin-induced ferroptosis.

To confirm the involvement of Suv39h1 in hemin-induced ferroptosis, chaetocin, an inhibitor of

Suv39h1/2, was used to inhibit the level of H3K9me3 pharmacologically. PI staining showed that hemin treatment increased the percentage of PI⁺ cells, while co-treatment with chaetocin further increased the percentage of PI⁺ cells (Figure 2(p) and (q)). Meanwhile, the cells were rescued when co-treated with DFO or Fer-1 (Figure 2(r) and Figure S1A). The level of lipid ROS also increased after hemin treatment, while more lipid ROS accumulated after co-treatment with chaetocin. The ferroptosis inhibitor DFO and Fer-1 suppressed lipid ROS accumulation induced by hemin and chaetocin stimulation (Figure 2(s) and Figure S1B). These results indicated that H3K9me3 plays a neuronal protective role in hemin induced ferroptosis in N2A cells.

H3K9me3 represses the expression of *Tfr1* transcriptionally

To further investigate how the increased H3K9me3 level regulates ferroptosis, we performed ChIP-Seq to screen potential target genes of H3K9me3. Figure 3(a) showed the genomic distribution of H3K9me3, which preferred to mark intergenic and intron regions on the genome in both vehicle- and hemin-treated N2A cells (Figure 3(a)). GO analyses indicated that H3K9me3 antibody-immunoprecipitated genes were enriched in several different terms, including catalytic activity, signal transducer activity, transcription factor activity, *etc.* (Figure 3(b)). Among the lists of vehicle- and H3K9me3-enriched genes (supplementary tables 1 and 2), we noticed a prominent enrichment of H3K9me3 at up- and downstream of the transcription start site (TSS) of *Tfr1* (also named as *Tfrc*), the gene coding transferrin receptor 1 (TFR1) which imports transferrin-bound iron into cells (Figure 3(c)). ChIP assays were carried out to confirm the alteration of H3K9me3 level on the promoter region (primer *Tfr1*-1#) and gene body (primer *Tfr1*-2#) of *Tfr1* in N2A cells with or without hemin treatment. Results of the agarose electrophoresis (Figure 3(d)) and Real-time PCR following ChIP (Figure 3(e) and (f)) both showed that treatment with hemin significantly increased the level of H3K9me3 at both the promoter and the gene body of *Tfr1*. Consistent with these data, compared with the vehicle group, hemin significantly reduced the mRNA level (Figure 3(g)) and protein level (Figure 3(h) and (i)) of *Tfr1* time-dependently. In addition, we compared the levels of H3K9me3, *Tfr1* mRNA, and TFR1 protein in N2A cells at each time point after hemin treatment. We found that while hemin treatment increased the level of H3K9me3 in N2A cells, it decreased the *Tfr1* mRNA and protein levels correspondingly (Figure 3(j)).

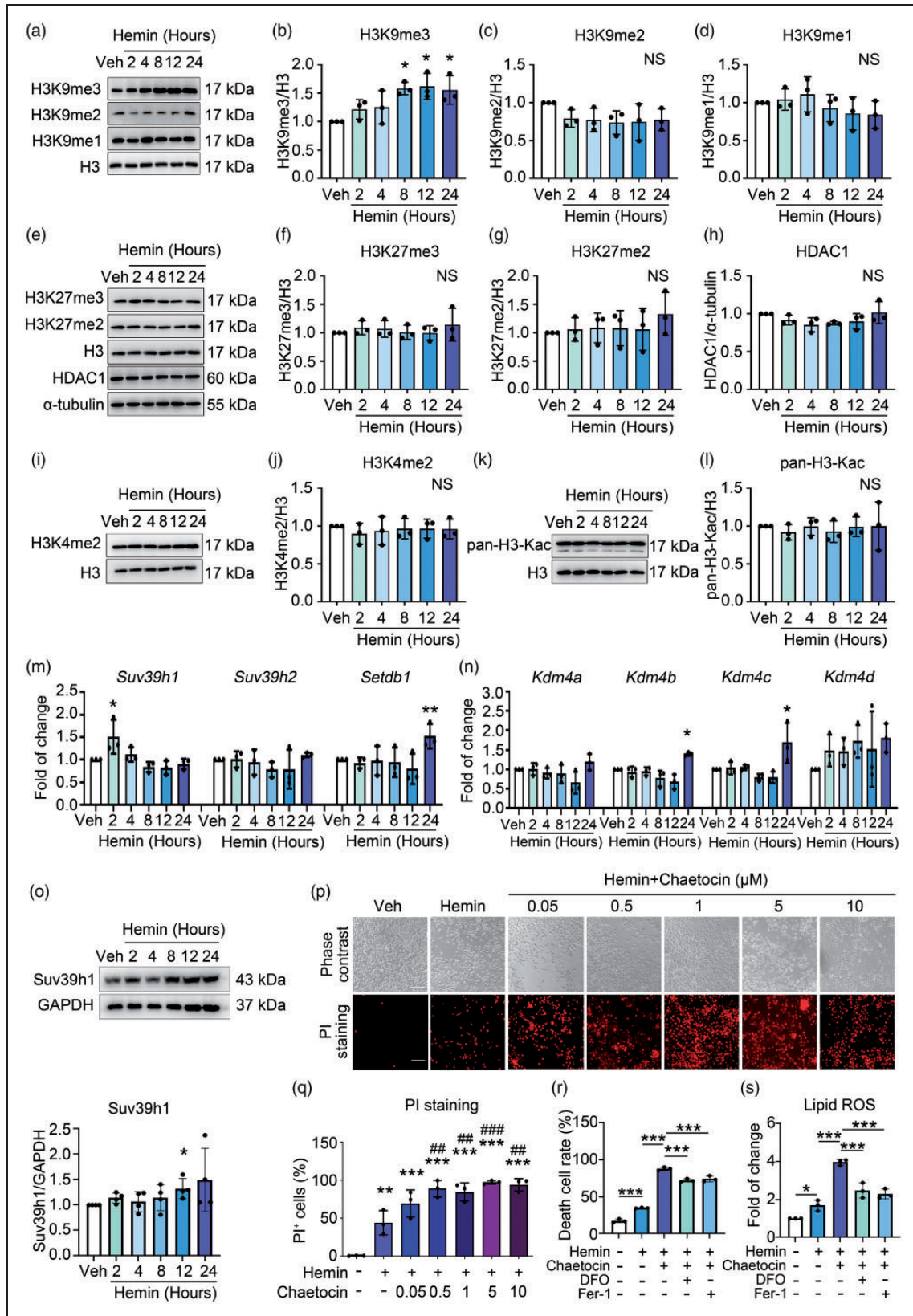


Figure 2. Suv39h1-mediated H3K9me3 elevation protects against hemin-induced neuronal ferroptosis. (a–l) N2A cells were treated with hemin or vehicle as indicated, and the levels of different histone modifications were assessed using Western blot. α-tubulin serves as an internal control. Representative images (a, e, i, k) and quantifications (b–d, f–h, j, l) are shown. (m, n) N2A cells were treated as Continued.

These data strongly suggested that hemin induced decrement of *Tfr1* expression was through up-regulation of H3K9me3. Therefore, we incubated cells with hemin with or without Suv39h1/2 inhibitor chaetocin. Compared with the vehicle group, hemin-induced increment of H3K9me3 level and decrement of TFR1 protein level, which were totally reversed by the addition of chaetocin (Figure 3(k) to (m)).

As TFR1 and TFR2 (encoded by the *Tfr2* gene) have similar functions, and TFR1 is widely expressed in mammalian cells,²⁶ while TFR2 is mainly expressed in liver and red blood cells.²⁷ We next assessed the mRNA expression of *Tfr2* and other related genes in iron metabolism and the xCT/GPx4 pathway. As shown in Figure 4(a), hemin treatment neither changed the mRNA expression of *Tfr2*, nor the Ferritin encoding genes *Fth1* and *Ftl1* at earlier time points. Additionally, the mRNA level of *Slc7a11* (the gene that encodes xCT) increased significantly at later time points of hemin treatment, whereas the mRNA level of *Gpx4* did not change markedly (Figure 4(b)). Furthermore, Western blot analyses showed that the protein levels of Ferritin, xCT, and GPx4 increased at 24 h after treating with hemin (Figure 4(c) and (d)). Consistent with the inhibition of TFR1, the intracellular level of transferrin gradually decreased post hemin treatment, which was most significant at 24 h (Figure 4 (e) and (f)). These results suggested that *Tfr1* was the most probable important target of H3K9me3 among those ferroptosis-related genes tested.

H3K9me3 represses *Tfr1* to protect against ferroptosis in N2A cells

To further confirm that H3K9me3 dictates ferroptosis by transcriptionally regulating *Tfr1*, we knocked down the expression of *Tfr1* (Figure 5(a) and (b)). The intracellular Fe²⁺ increased after hemin stimulation while silencing *Tfr1* reduced Fe²⁺ content at both the basal and hemin treated conditions (Figure 5(c)). We also knocked down the expression of *Suv39h1* (Figure 5 (d)), whereas the mRNA level of *Suv39h2* was not affected (Figure 5(e)). We found that cells transfected with *Suv39h1* siRNA significantly increased the level of hemin-induced lipid ROS, while silencing of *Tfr1* notably reduced the lipid ROS level induced by hemin treatment (Figure 5(f) and (g)). Consistent with results of

lipid ROS, PI staining revealed that knocking down of *Suv39h1* aggravated hemin-induced cell death, while *Tfr1* siRNAs decreased the percentage of PI⁺ cells (Figure 5(h) and (i)).

Inhibition of GPx4 activity is one of the core mechanisms underpinning hemin induced neuronal ferroptosis.²⁸ We next incubated RSL3-treated cells with or without chaetocin. The results showed that compared with the vehicle group, RSL3 treatment alone increased the intracellular lipid ROS levels (Figure 5(j) and (k)) and the percentage of PI⁺ cells (Figure 5(l) and (m)), whereas chaetocin aggravated the intracellular lipid ROS accumulation (Figure 5(j) and (k)) and cell death (Figure 5(l) and (m)) caused by RSL3. Furthermore, compared with the scramble siRNA-transfection treatment, *Suv39h1* siRNA treatment caused severer cell death, while *Tfr1* siRNA treatment attenuated cell death induced by RSL3 (Figure 5(n) and (o)). Altogether, these results indicated that Suv39h1 mediated H3K9me3 represses *Tfr1* at the transcription level to protect against neuronal ferroptosis.

Suv39h1-H3K9me3 mediated repression of TFR1 plays a protective role after ICH

To further test whether Suv39h1-H3K9me3 mediated repression of TFR1 also works *in vivo*, we used a murine model of ICH. The alteration dynamics for the level of Suv39h1 and H3K9me3 were examined with ICH progression. We first examined the level of Suv39h1 and H3K9me3 at day 1 and 3 post ICH with immunofluorescence staining. Different from *in vitro* results, the global average level of Suv39h1 and H3K9me3 were both decreased (Figure 6(a), (b), (d) and (e)), together with the reduction of neuronal localization for Suv39h1 or H3K9me3 as demonstrated with Manders' colocalization coefficient between Suv39h1 or H3K9me3 and the neuron marker NeuN (Figure 6 (c) and (f)). On the contrary, the level of TFR1 was increased as determined with western blot and immunofluorescence, which was most prominent at day 1 after ICH (Figure 6(g) to (i)). The number of degenerating neurons around the lesion has been reported to peak at 24 hours after ICH,⁵ we postulated that if Suv39h1 mediated H3K9me3 dictates neuronal ferroptosis, their level change should precede massive

Figure 2. Continued.

indicated. Total mRNA was extracted and Real-time RT-PCR was performed. *GAPDH* serves as an internal control. (o) N2A cells were treated as indicated. The protein level of Suv39h1 was detected using Western blot (up) and quantified (down). (p, q) N2A cells were treated as indicated, and PI staining was performed. Representative images (p) and quantifications (q) are shown. (r, s) Cell death and lipid ROS were detected. Results are shown as scatter plots (Mean ± SD). n = 3–4 independent experiments. One-way ANOVA followed by Tukey's multiple comparisons tests (b–d, f–h, j, l, m, n, q, r, s) or two-tailed t test (o) was used. *p < 0.05, **p < 0.01, ***p < 0.001 vs vehicle; ###p < 0.01, ####p < 0.001 vs. Hemin; NS, not significant. Scale bar: 100 μm.

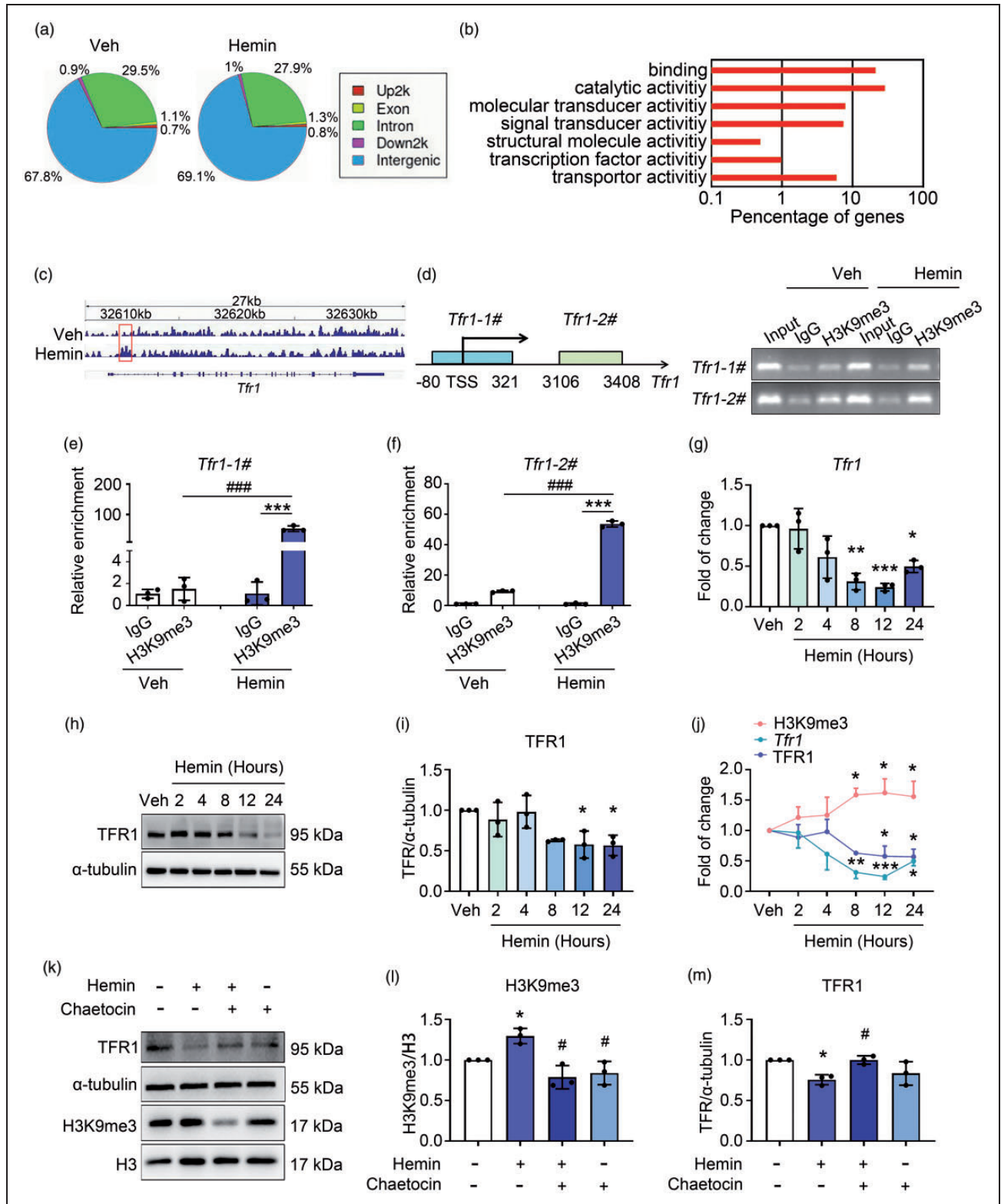


Figure 3. H3K9me3 represses *Tfr1* expression during neuronal ferroptosis. (a) Genomic distribution of the H3K9me3 in vehicle and hemin treated N2A cells that detected with ChIP-Seq. (b) GO analyses of annotated targets of H3K9me3 histone modification in hemin treated group based on ChIP-Seq data. (c) Integrated genome viewer of H3K9me3 ChIP-seq tracings for the *Tfr1* locus in vehicle and Hemin groups. Increased enrichment of H3K9me3 signal on the *Tfr1* gene is shown in red rectangle. (d) Left: the schematic diagram shows the primers designed to perform ChIP assays at the *Tfr1* locus. TSS, transcription start site. Right: DNA

Continued.

ferroptosis at day 1. To test this hypothesis, we further detected the level of Suv39h1 and H3K9me3 at earlier time points before 24 h post ICH with immunofluorescence. This time, consistent with the *in vitro* data, the average level of Suv39h1 and H3K9me3 both gradually increased at 6 h and 12 h post ICH, with the change at 12 h reaching peak and showing statistical significance (Figure S2A-D). These results indicate that early changes of Suv39h1 and H3K9me3 may contribute to neuronal ferroptosis in the ICH model. We also compared the relative level of Suv39h1 in neurons (NeuN⁺), astrocytes (GFAP⁺), microglia (Iba-1⁺) and oligodendrocytes (Olig2⁺) with immunostaining assays, where the neurons showed the highest expression in both Sham and ICH groups (Figures S3A-D).

To further explore the function of neuronal Suv39h1-mediated H3K9me3 in ICH, we knocked down the expression of *Suv39h1* in ICH mice by intracerebroventricular injection of *Suv39h1*-specific and scramble siRNAs. The expression of Suv39h1 was decreased the most in neurons as demonstrated with decreased colocalization between NeuN and Suv39h1 around the hematoma, while its colocalization coefficients in glial cells were less affected (Figure 6(j) and S3E-H). Compared with scramble group, the level of H3K9me3 was decreased (Figure 6(k)) while TFR1 increased (Figure 6(l)) with *Suv39h1* knockdown. The level of malondialdehyde (MDA), one main product of lipid peroxidation,^{29,30} was measured to represent ferroptosis in ICH tissue, which showed overt increment with knocking down *Suv39h1* (Figure 6(m)). To be of pathophysiological importance, neurologic functions were assessed with neurologic deficit score, forelimb placing test and hindlimb placing test, and the results showed that the neurological deficit was even worse, and forelimb and hindlimb movement were more severely impaired after knocking down *Suv39h1* (Figure 6(n) to (p)).

Discussion

Labile iron accumulation promotes ferroptosis, and genes involved in iron metabolism are vital regulators of ferroptosis.²⁹ Transferrin receptors (TFRs) are cell surface receptor proteins encoded by *Tfr1* or *Tfr2*,

whose main function is incorporating Fe³⁺-transferrin (TF) complex into cells or regulating systematic iron homeostasis and erythropoiesis, respectively.³¹ The level of TFR1 was much more sensitive to alterations of intracellular iron levels. When the cellular iron increases, the expression TFR1 decreases in a negative feedback manner, and *vice versa*.³¹ It thus no wonder that TFR1 was down regulated upon hemin treatment, which significantly increases the level of intracellular iron. In line with its iron-uptake function, TFR1 has been reported to play an important role in ferroptosis promotion in several disease models, including myocardial I/R injury,³² central presbycusis,³³ and cerebral ischemic injury.³⁴ In those models, the level of TFR1 can be directly regulated in a p53-dependent manner at the transcription level and by the upregulation of iron regulatory protein 2 (IRP-2) at the translation level, or be regulated by GPx4 and FTH1 indirectly.^{33,34} Interestingly, in some types of cancer like high-grade ovarian cancer and MYCN-amplified neuroblastoma, TFR1 is overexpressed, and underlies the predilection of these cells to a high level of intracellular iron and renders them more susceptible to inhibition of the system χ_c^- /glutathione (GSH) system.^{35,36} Thus, the role and regulation of TFR1 in ferroptosis is complicated in various cells/diseases, but how epigenetics participate in the regulation of *Tfr1* in ferroptosis was unknown.

In our study, *Tfr1* was down-regulated during hemin-induced neuronal ferroptosis, and further down-regulating its expression level attenuated ferroptosis notably. Therefore, down-regulation of *Tfr1* acted as an endogenous self-protective mechanism to buffer intracellular iron overload induced by hemin degradation. Consistent with this hypothesis, treating cells with chaetocin, an inhibitor of methyltransferases Suv39h1/2 of H3K9me3, upregulated *Tfr1* expression level, and aggravated ferroptosis. *In vivo* model showed similar results that down-regulation of *Tfr1* through Suv39h1 mediated H3K9me3 protects neurons from ferroptosis post ICH.

Chromatin remodeling,³⁷⁻³⁹ DNA methylations,⁴⁰⁻⁴² histone modifications,^{40,43,44} and non-coding RNAs⁴⁵⁻⁴⁸ regulate ferroptosis in cancer cells. However, other than a study where inhibitors of HDAC induce neuronal

Figure 3. Continued.

electrophoresis using agarose gels followed by ChIP assays. (e, f) ChIP assays were analyzed with Real-time qPCR. Results are expressed as fold enrichment to IgG. (g) N2A cells were treated as indicated, and the mRNA level of *Tfr1* was assessed with Real-time RT-PCR. *GAPDH* serves as an internal control. (h, i, k-m) N2A cells were treated as indicated, and proteins were extracted for Western blot. α -tubulin serves as an internal control. Representative images (h, k) and quantifications (i, l, m) are shown. (j) The levels of H3K9me3, *Tfr1* mRNA, and TFR1 protein in N2A cells at different time points upon hemin or vehicle treatment were compared. Results are shown as scatter plots or line charts (Mean \pm SD). n = 3 independent experiments. Two-way ANOVA followed by Tukey's multiple comparisons tests (e, f) or One-way ANOVA followed by Tukey's multiple comparisons tests (g, i, j, l, m) was used. **p* < 0.05, ***p* < 0.01, ****p* < 0.001 vs vehicle or corresponding IgG. #*p* < 0.05, vs Hemin.

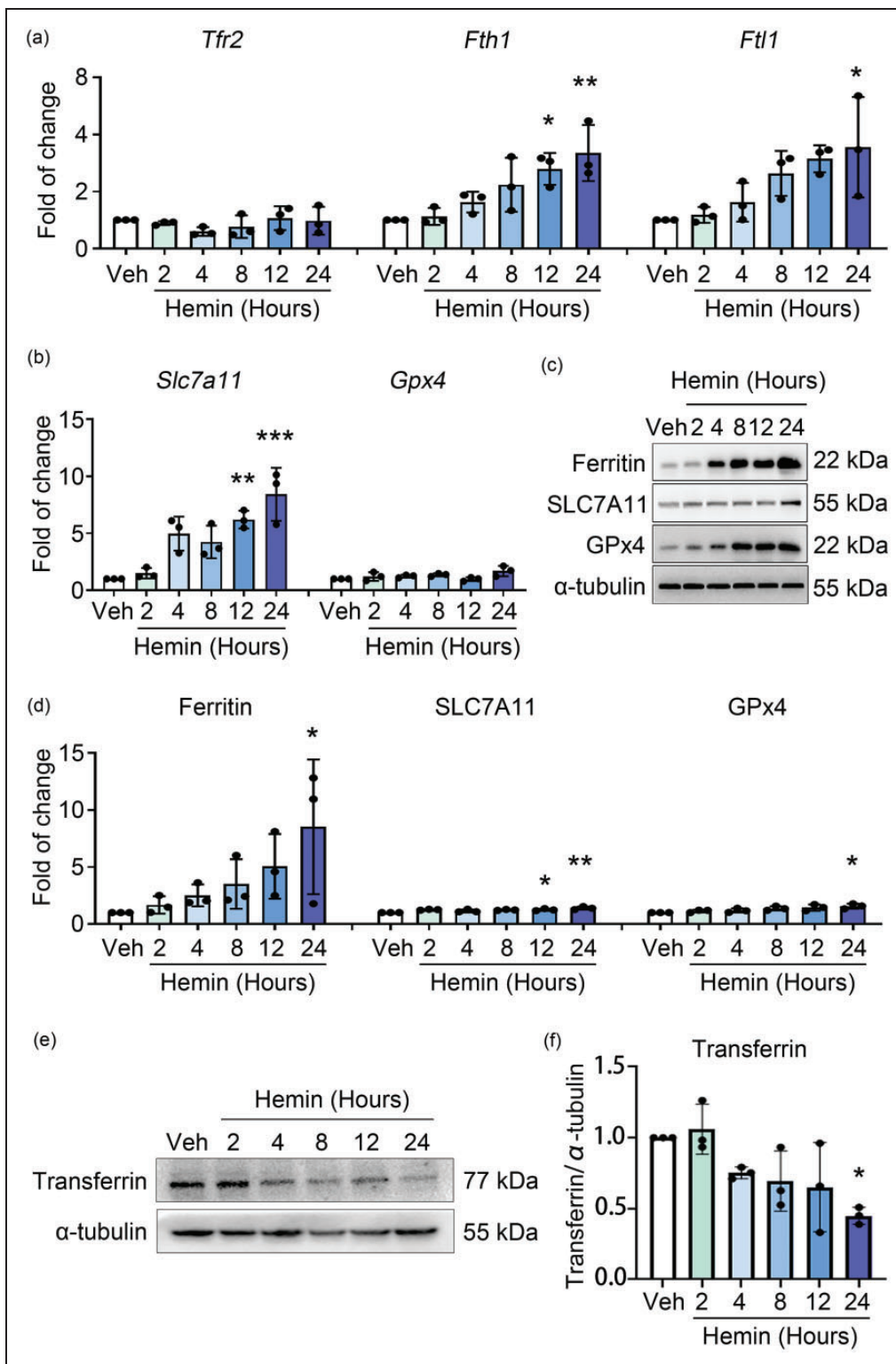


Figure 4. Genes in iron-metabolism or the xCT/GPx4 pathway other than *Tfr1* were not repressed by H3K9me3 during hemin-induced ferroptosis. (a, b) N2A cells were treated as indicated. Total mRNA was extracted and Real-time RT-PCR was performed. The mRNA levels of genes in iron metabolism (a) and xCT/GPx4 pathway (b) are shown. *GAPDH* serves as an internal control. (c, d) N2A cells were treated as indicated. Proteins were extracted and Western blot was performed. α -tubulin serves as an internal control. Representative images (c) and quantifications (d) are shown. (e, f) N2A cells were treated as indicated. The level of transferrin was detected by using Western blot (e) and quantified (f). Results are shown as scatter plots (Mean \pm SD). $n = 3$ independent experiments. One-way ANOVA (a, b, f) or Kruskal-Wallis test (d) followed by Tukey's or Dunn's multiple comparisons tests was used. * $p < 0.05$, ** $p < 0.01$, *** $p < 0.001$ vs vehicle.

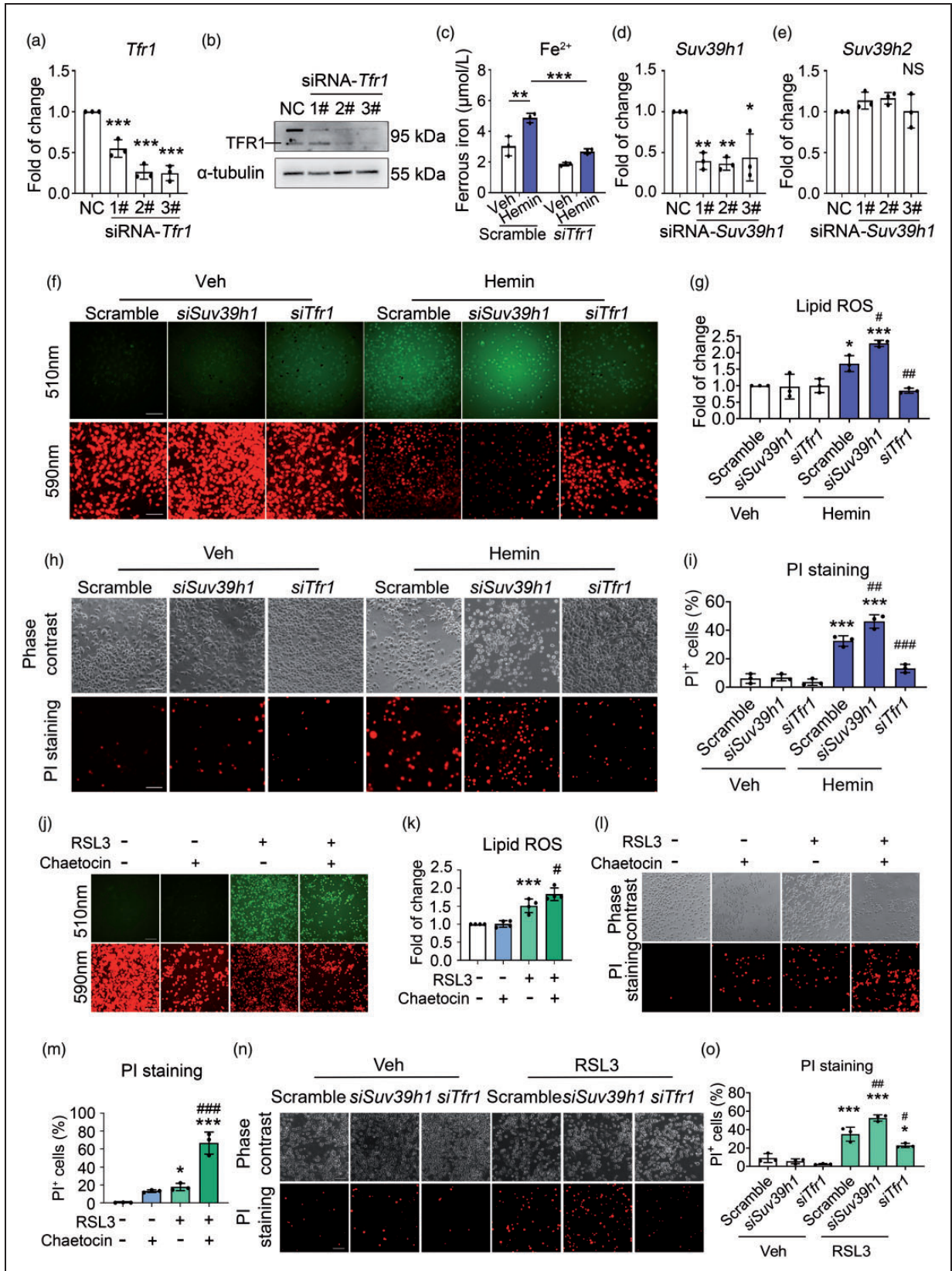


Figure 5. Suv39h1-mediated H3K9me3 protects against hemin- and RSL3-induced neuronal ferroptosis by repressing *Tfr1*. (a, b) N2A cells were transfected with Scramble or *Tfr1* siRNA for 48 h. (a) Total mRNA was extracted, and Real-time RT-PCR was performed. *GAPDH* serves as an internal control. (b) Proteins were extracted and Western blot was performed. α -tubulin serves as an internal control. (Continued.)

ferroptosis by deacetylation H4ac,⁴⁹ how epigenetic regulates ferroptosis in neurons remains to be explored. In this study, through a screening of histone modifications in hemin-treated neuronal cells, we focused on the role of H3K9me3 in mediating ferroptosis. H3K9me3 is the best-known histone modification for its role in facilitating constitutive heterochromatin formation and in the repression of repetitive DNA.¹⁵ Three methyltransferases and 4 demethylases are responsible for the dynamic changes of H3K9me3 level.⁵⁰ In our study, we found that the level of global H3K9me3 showed a concomitant upregulation during hemin treatment, and the upregulation of *Suv39h1* mRNA was observed before H3K9me3 accumulation, suggesting its contribution to H3K9me3. How hemin treatment increases the level of *Suv39h1* is currently unknown. To be of functional importance, decreasing global H3K9me3 through pharmacologic and genetic approaches towards *Suv39h1* effectively aggravated hemin- and RSL3-induced ferroptosis. Consistent with our observation, a recent report indicates that *Suv39h1* deficiency induces ferroptosis in clear cell renal cell carcinoma through targeting *DPP4* (dipeptidyl-peptidase-4),⁵¹ suggesting protection against ferroptosis in different cell types. *Suv39h1*-mediated H3K9me3 was supposed to regulate *Tfr1* and lots of other genes, however, repressing *Tfr1* gene expression may be the one of the most important functions of H3K9me3 increment in restricting neuronal ferroptosis.

Interestingly, all methyltransferases of H3K9me3, including *Suv39h1*, cannot recognize specific DNA sequences of target genes to bind directly. Therefore, additional scaffold proteins or transcription factors are needed, such as Krüppel-associated box (KRAB)-containing zinc-finger proteins (KRAB-ZFPs)⁵² or retinoblastoma (Rb) protein.⁵³ In the future study, how *Suv39h1* recognizes and binds to *Tfr1*, and mediates H3K9me3 increment at *Tfr1* promoter and gene body are worthy to be investigated. Meanwhile, whether inhibition of *Tfr1* by H3K9me3 functions as common mechanism that underlies the feedback down-regulation of *Tfr1* upon increased iron level in other pathophysiological models also needs further investigation. Furthermore, besides H3K9me3, other epigenetic modifications must also participate in the neuronal ferroptosis in orchestration with H3K9me3. Although

other histone modifications levels did not show significant global alterations in our screening, the redistribution of these modifications on the chromosome may also interfere with hemin-induced ferroptosis.

Although multiple differences exist between experimental conditions, like difference in cellular context (neuron only *in vitro* versus neuron and glia cells, *etc. in vivo*), and difference in stimuli types (hemin only *in vitro* versus intracranial pressure, and many types of toxins including hemin *in vivo*), both *in vitro* and *in vivo* results showed that *Suv39h1* and H3K9me3 repressed the expression of *Tfr1*, and more importantly, early up-regulation of *Suv39h1*-mediated H3K9me3 before massive ferroptosis played a protective role for the neuron. These results also indicated that early interventions targeting *Suv39h1*-H3K9me3-TFR1 axis may represent a novel therapeutic option for ICH.

Epigenetic regulation of neuronal ferroptosis might cross talk with other protective or destructive mechanisms during cerebral hemorrhage injury. For example, inhibition of HDAC could reduce white matter damage after ICH by modulating the polarization of microglia and macrophages and improve ICH-mediated neuroinflammation.⁵⁴ However, inhibition of HDAC induces neuronal ferroptosis,⁴⁹ how to properly manipulating those mechanisms to most benefit the whole brain or organism will need more intensive investigation. The mechanism of ferroptosis in tumors has been extensively studied, some of which also works in the neurons. Acyl-CoA synthetase long chain family member 4 (ACSL4), a promoter of ferroptosis in tumor cells, also exacerbate early brain damage caused by subarachnoid hemorrhage by mediating ferroptosis.⁵⁵ The interrelationship between these metabolic and epigenetic specific enzymes in neuronal ferroptosis during ICH also needs further investigation, which may hold powerful therapeutic potentials for ICH treatment.

In our *in vivo* experimental design, we delivered siRNAs intracerebroventricularly to reduce the *Suv39h1* expression. We knocked down *Suv39h1* in neurons with less perturbation in the glial cells, possibly due to their different expression levels. From a point view of basic research, the use of neuronal conditional knockout mice or the expression of

Figure 5. Continued.

internal control. Representative images are shown. (c) The intracellular ferrous iron was detected. (d, e) N2A cells were transfected with Scramble or *Suv39h1* siRNA for 48 h. Total mRNA was extracted, and Real-time RT-PCR was performed. *GAPDH* serves as an internal control. (f–o) N2A cells were treated as indicated. Lipid ROS that were assessed using BODIPY 581/591 C11 dye (f, g, j, k), and cell death that were assessed using PI staining (h, i, l–o). Representative images (f, h, j, l, n) and quantifications (g, i, k, m, o) are shown. Results are shown as scatter plots (Mean ± SD). n = 3 independent experiments. One-way ANOVA followed by Tukey's multiple comparisons tests (a, d, e, k, m) or Two-way ANOVA followed by Tukey's multiple comparisons tests (c, g, i, o) was used. **p* < 0.05, ***p* < 0.01, ****p* < 0.001 vs vehicle. #*p* < 0.05, ###*p* < 0.01, ####*p* < 0.001 vs. Hemin, RSL3, or Scramble; NS: not significant. Scale bar: (f, h, j, l, n) 100 μm.

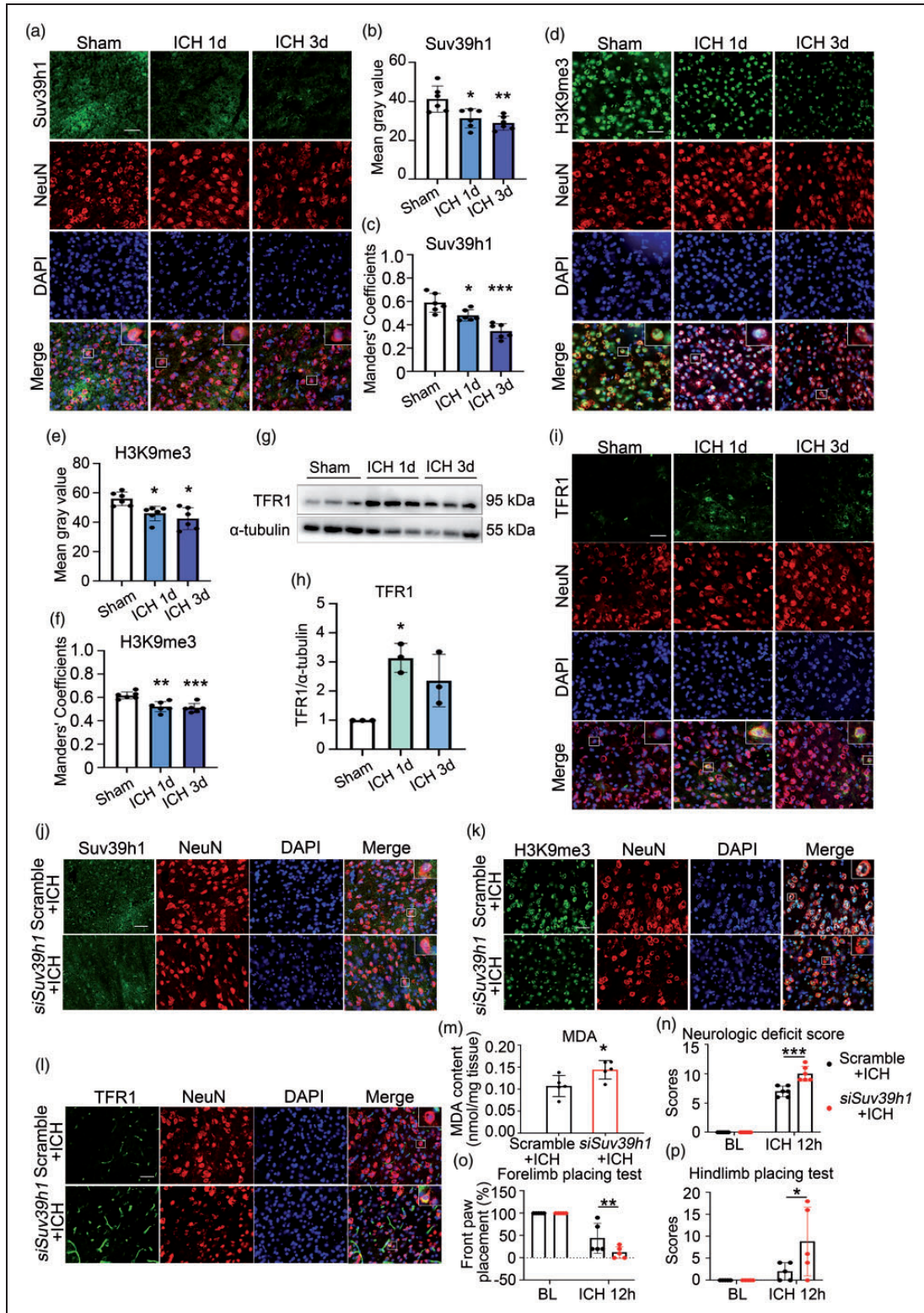


Figure 6. Suv39h1-mediated H3K9me3 regulated ferroptosis after ICH. (a–f) Brain slices obtained at day 1 and 3 post ICH were stained with Suv39h1, H3K9me3, NeuN antibody and DAPI (a, d). The mean fluorescence intensity of Suv39h1 and H3K9me3 were quantified respectively (b, e). The Manders' Colocalization Coefficients (M1) were calculated (c, f). (g, h) The protein of TFR1 was detected from ipsilateral striatum using Western blot (g) and quantified (h). (i) Immunostaining was performed using TFR1 antibody at 1 day and 3 days post ICH. (j–l) Immunostaining was performed using Suv39h1 (j), H3K9me3 (k) or TFR1 antibody (l) at day 3 post ICH. (m) MDA content was measured at day 3 after ICH. (n–p) Neurological function was assessed at 12 h post ICH. Results are shown as scatter plots (Mean \pm SD). $n = 6$ images from 3 mice (b, c, e, f). $n = 3$ mice (h). $n = 5$ –6 mice (m–p). One-way ANOVA (b, c, f, h, n–p) or Kruskal-Wallis test (e) followed by Tukey's or Dunn's multiple comparisons tests, respectively or two-tailed t test (m) was used. * $p < 0.05$, ** $p < 0.01$, *** $p < 0.001$ vs Sham or Scramble or baseline (BL) group. Scale bar: (a, d, i, j, k, l) 75 μ m.

shRNAs/siRNAs in viral vectors under the control of a promoter like Syn1 are more specific strategies to address the *in vivo* involvement of Suv39h1 in ICH, as will be demonstrated in the future. Consistent with our method, several recent papers also used siRNA to examine the function of target genes, and successfully decreased the expression of genes in the cell types of interest *in vivo*.^{56,57} With respect to the translation from basic research to clinical application, direct siRNA delivery in non-viral vectors such as nanoparticles may be a better option, which should provide a more prompt and less toxic treatment for ICH cases.⁵⁸ Further studies in the two directions above would be worthwhile to better elucidate the function of the neuronal Suv39h1-H3K9me3-TFR1 axis during ICH and their potential clinical applications.

In summary, Suv39h1 mediated H3K9me3 repressed *Tfr1* gene expression in neurons. Attenuation of Suv39h1-mediated H3K9me3 aggravated hemin-induced neuronal ferroptosis and ICH damage. Our findings shed new light on ferroptosis' molecular mechanisms and may help improve patient recovery after ICH.

Funding

The author(s) disclosed receipt of the following financial support for the research, authorship, and/or publication of this article: this work was supported by the National Natural Science Foundation of China (32070735 to Q. Li, 81971037 to F. Yang).

Availability of data and materials

All data generated or analyzed during this study are included in this published article and its supplementary information files.

Acknowledgements

We thank Dr. Zhiqing Xu from Capital Medical University for kindly providing the N2A cell line. We thank Dr. Xi Wang from Capital Medical University for providing Suv39h1/2 antibodies. We thank Dr. Lin Shan from Capital Medical University for providing histone modification related antibodies. We thank Wenzhu Wang, Ting Li and Fan Bai from Chinese Institute of Rehabilitation Science, China Rehabilitation Science Institute, Beijing, China, and Beijing Key Laboratory of Neural Injury and Rehabilitation, China Rehabilitation Research Center, Beijing, China for providing technical support.

Declaration of conflicting interests


The author(s) declared no potential conflicts of interest with respect to the research, authorship, and/or publication of this article.

Authors' contributions

Lan T., Hu L., Zhang C., and Li Q. designed the experiments, wrote, and revised the manuscript. Lan T. and Hu L.

performed experiments; Lan T., Hu L., Sun T., Wang X., Xiao Z., Shen D., Wu W., Luo Z., Wei C., Wang X., Liu M., Guo Y., Wang L., Wang Y., Lu Y., Yu Y., Yang F., Zhang C., and Li Q. collected and analyzed data. All authors have agreed on the final version to be published.

ORCID iD

Yamei Wang  <https://orcid.org/0000-0002-8240-3991>

Supplemental material

Supplemental material for this article is available online.

References

1. Keep RF, Hua Y and Xi G. Intracerebral haemorrhage: mechanisms of injury and therapeutic targets. *Lancet Neurol* 2012; 11: 720–731.
2. van Asch CJ, Luitse MJ, Rinkel GJ, et al. Incidence, case fatality, and functional outcome of intracerebral haemorrhage over time, according to age, sex, and ethnic origin: a systematic review and meta-analysis. *Lancet Neurol* 2010; 9: 167–176.
3. Graeber MB, Raivich G and Kreutzberg GW. Increase of transferrin receptors and iron uptake in regenerating motor neurons. *J Neurosci Res* 1989; 23: 342–345.
4. Zhu X, Tao L, Tejima-Mandeville E, et al. Plasmalemma permeability and necrotic cell death phenotypes after intracerebral hemorrhage in mice. *Stroke* 2012; 43: 524–531.
5. Li Q, Han X, Lan X, et al. Inhibition of neuronal ferroptosis protects hemorrhagic brain. *JCI Insight* 2017; 2: e90777.
6. Gao Y, Ma L, Luo CL, et al. IL-33 Exerts neuroprotective effect in mice intracerebral hemorrhage model through suppressing inflammation/apoptotic/autophagic pathway. *Mol Neurobiol* 2017; 54: 3879–3892.
7. Dixon SJ, Lemberg KM, Lamprecht MR, et al. Ferroptosis: an iron-dependent form of nonapoptotic cell death. *Cell* 2012; 149: 1060–1072.
8. Yang WS and Stockwell BR. Ferroptosis: death by lipid peroxidation. *Trends Cell Biol* 2016; 26: 165–176.
9. Yang WS, SriRamaratnam R, Welsch ME, et al. Regulation of ferroptotic cancer cell death by GPX4. *Cell* 2014; 156: 317–331.
10. Kwon MY, Park E, Lee SJ, et al. Heme oxygenase-1 accelerates erastin-induced ferroptotic cell death. *Oncotarget* 2015; 6: 24393–24403.
11. Zille M, Karuppagounder SS, Chen Y, et al. Neuronal death after hemorrhagic stroke in vitro and in vivo shares features of ferroptosis and necroptosis. *Stroke* 2017; 48: 1033–1043.
12. Ren H, Han R, Chen X, et al. Potential therapeutic targets for intracerebral hemorrhage-associated inflammation: an update. *J Cereb Blood Flow Metab* 2020; 40: 1752–1768.
13. Jenuwein T and Allis CD. Translating the histone code. *Science* 2001; 293: 1074–1080.

14. Ninova M, Fejes Toth K and Aravin AA. The control of gene expression and cell identity by H3K9 trimethylation. *Development* 2019; 146: dev181180.
15. Becker JS, Nicetto D and Zaret KS. H3K9me3-dependent heterochromatin: barrier to cell fate changes. *Trends Genet* 2016; 32: 29–41.
16. Schultz DC, Ayyanathan K, Negorev D, et al. SETDB1: a novel KAP-1-associated histone H3, lysine 9-specific methyltransferase that contributes to HP1-mediated silencing of euchromatic genes by KRAB zinc-finger proteins. *Genes Dev* 2002; 16: 919–932.
17. Nicetto D, Donahue G, Jain T, et al. H3K9me3-heterochromatin loss at protein-coding genes enables developmental lineage specification. *Science* 2019; 363: 294–297.
18. Rea S, Eisenhaber F, O'Carroll D, et al. Regulation of chromatin structure by site-specific histone H3 methyltransferases. *Nature* 2000; 406: 593–599.
19. Loh YH, Zhang W, Chen X, et al. Jmjd1a and Jmjd2c histone H3 Lys 9 demethylases regulate self-renewal in embryonic stem cells. *Genes Dev* 2007; 21: 2545–2557.
20. Couture JF, Collazo E, Ortiz-Tello PA, et al. Specificity and mechanism of JMJD2A, a trimethyllysine-specific histone demethylase. *Nat Struct Mol Biol* 2007; 14: 689–695.
21. Sabbattini P, Canzonetta C, Sjoberg M, et al. A novel role for the Aurora B kinase in epigenetic marking of silent chromatin in differentiated postmitotic cells. *EMBO J* 2007; 26: 4657–4669.
22. Puschendorf M, Terranova R, Boutsma E, et al. PRC1 and Suv39h specify parental asymmetry at constitutive heterochromatin in early mouse embryos. *Nat Genet* 2008; 40: 411–420.
23. Wood JG, Hillenmeyer S, Lawrence C, et al. Chromatin remodeling in the aging genome of Drosophila. *Aging Cell* 2010; 9: 971–978.
24. Wiencke JK, Zheng S, Morrison Z, et al. Differentially expressed genes are marked by histone 3 lysine 9 trimethylation in human cancer cells. *Oncogene* 2008; 27: 2412–2421.
25. Xiao Z, Shen D, Lan T, et al. Reduction of lactoferrin aggravates neuronal ferroptosis after intracerebral hemorrhagic stroke in hyperglycemic mice. *Redox Biol* 2022; 50: 102256.
26. Gammella E, Buratti P, Cairo G, et al. The transferrin receptor: the cellular iron gate. *Metallomics* 2017; 9: 1367–1375.
27. Kawabata H, Yang R, Hiramata T, et al. Molecular cloning of transferrin receptor 2. A new member of the transferrin receptor-like family. *J Biol Chem* 1999; 274: 20826–20832.
28. Karuppagounder SS, Alin L, Chen Y, et al. N-acetylcysteine targets 5 lipoxygenase-derived, toxic lipids and can synergize with prostaglandin E2 to inhibit ferroptosis and improve outcomes following hemorrhagic stroke in mice. *Ann Neurol* 2018; 84: 854–872.
29. Jiang X, Stockwell BR and Conrad M. Ferroptosis: mechanisms, biology and role in disease. *Nat Rev Mol Cell Biol* 2021; 22: 266–282.
30. Su LJ, Zhang JH, Gomez H, et al. Reactive oxygen species-induced lipid peroxidation in apoptosis, autophagy, and ferroptosis. *Oxid Med Cell Longev* 2019; 2019: 5080843.
31. Kawabata H. Transferrin and transferrin receptors update. *Free Radic Biol Med* 2019; 133: 46–54.
32. Tang LJ, Zhou YJ, Xiong XM, et al. Ubiquitin-specific protease 7 promotes ferroptosis via activation of the p53/TfR1 pathway in the rat hearts after ischemia/reperfusion. *Free Radic Biol Med* 2021; 162: 339–352.
33. Chen X, Li D, Sun HY, et al. Relieving ferroptosis may partially reverse neurodegeneration of the auditory cortex. *FEBS J* 2020; 287: 4747–4766.
34. Li G, Li X, Dong J, et al. Electroacupuncture ameliorates cerebral ischemic injury by inhibiting ferroptosis. *Front Neurol* 2021; 12: 619043.
35. Floros KV, Cai J, Jacob S, et al. MYCN-amplified neuroblastoma is addicted to iron and vulnerable to inhibition of the system Xc-/glutathione axis. *Cancer Res* 2021; 81: 1896–1908.
36. Basuli D, Tesfay L, Deng Z, et al. Iron addiction: a novel therapeutic target in ovarian cancer. *Oncogene* 2017; 36: 4089–4099.
37. Jiang Y, He Y, Liu S, et al. Chromatin remodeling factor lymphoid-specific helicase inhibits ferroptosis through lipid metabolic genes in lung cancer progression. *Chin J Cancer* 2017; 36: 82.
38. Mao C, Wang X, Liu Y, et al. A G3BP1-interacting lncRNA promotes ferroptosis and apoptosis in cancer via nuclear sequestration of p53. *Cancer Res* 2018; 78: 3484–3496.
39. Huang D, Li Q, Sun X, et al. CRL4(DCAF8) dependent opposing stability control over the chromatin remodeler LSH orchestrates epigenetic dynamics in ferroptosis. *Cell Death Differ* 2021; 28: 1593–1609.
40. Jiang Y, Mao C, Yang R, et al. EGLN1/c-Myc induced lymphoid-specific helicase inhibits ferroptosis through lipid metabolic gene expression changes. *Theranostics* 2017; 7: 3293–3305.
41. Zhang X, Sui S, Wang L, et al. Inhibition of tumor propeptant glutathione peroxidase 4 induces ferroptosis in cancer cells and enhances anticancer effect of cisplatin. *J Cell Physiol* 2020; 235: 3425–3437.
42. Lee JY, Nam M, Son HY, et al. Polyunsaturated fatty acid biosynthesis pathway determines ferroptosis sensitivity in gastric cancer. *Proc Natl Acad Sci U S A* 2020; 117: 32433–32442.
43. Zhang Y, Shi J, Liu X, et al. BAP1 links metabolic regulation of ferroptosis to tumour suppression. *Nat Cell Biol* 2018; 20: 1181–1192.
44. Zhang Y, Zhuang L and Gan B. BAP1 suppresses tumor development by inducing ferroptosis upon SLC7A11 repression. *Mol Cell Oncol* 2019; 6: 1536845.
45. Qi W, Li Z, Xia L, et al. LncRNA GABPB1-AS1 and GABPB1 regulate oxidative stress during erastin-induced ferroptosis in HepG2 hepatocellular carcinoma cells. *Sci Rep* 2019; 9: 16185.
46. Tomita K, Fukumoto M, Itoh K, et al. MiR-7-5p is a key factor that controls radioresistance via intracellular Fe(2+) content in clinically relevant radioresistant cells. *Biochem Biophys Res Commun* 2019; 518: 712–718.

47. Wang Z, Chen X, Liu N, et al. A nuclear long non-coding RNA LINC00618 accelerates ferroptosis in a manner dependent upon apoptosis. *Mol Ther* 2021; 29: 263–274.
48. Ma Q, Dai X, Lu W, et al. Silencing long non-coding RNA MEG8 inhibits the proliferation and induces the ferroptosis of hemangioma endothelial cells by regulating miR-497-5p/NOTCH2 axis. *Biochem Biophys Res Commun* 2021; 556: 72–78.
49. Zille M, Kumar A, Kundu N, et al. Ferroptosis in neurons and cancer cells is similar but differentially regulated by histone deacetylase inhibitors. *eNeuro* 2019; 6: 0263–18.
50. Shi Y and Whetstone JR. Dynamic regulation of histone lysine methylation by demethylases. *Mol Cell* 2007; 25: 1–14.
51. Wang J, Yin X, He W, et al. SUV39H1 deficiency suppresses clear cell renal cell carcinoma growth by inducing ferroptosis. *Acta Pharm Sin B* 2021; 11: 406–419.
52. Matsui T, Leung D, Miyashita H, et al. Proviral silencing in embryonic stem cells requires the histone methyltransferase ESET. *Nature* 2010; 464: 927–931.
53. Sdek P, Zhao P, Wang Y, et al. Rb and p130 control cell cycle gene silencing to maintain the postmitotic phenotype in cardiac myocytes. *J Cell Biol* 2011; 194: 407–423.
54. Yang H, Ni W, Wei P, et al. HDAC inhibition reduces white matter injury after intracerebral hemorrhage. *J Cereb Blood Flow Metab* 2021; 41: 958–974.
55. Qu XF, Liang TY, Wu DG, et al. Acyl-CoA synthetase long chain family member 4 plays detrimental role in early brain injury after subarachnoid hemorrhage in rats by inducing ferroptosis. *CNS Neurosci Ther* 2021; 27: 449–463.
56. Shen F, Xu X, Yu Z, et al. Rbfox-1 contributes to CaMKIIalpha expression and intracerebral hemorrhage-induced secondary brain injury via blocking micro-RNA-124. *J Cereb Blood Flow Metab* 2021; 41: 530–545.
57. You M, Long C, Wan Y, et al. Neuron derived fractalkine promotes microglia to absorb hematoma via CD163/HO-1 after intracerebral hemorrhage. *Cell Mol Life Sci* 2022; 79: 224.
58. Almarghalani DA, Boddu SHS, Ali M, et al. Small interfering RNAs based therapies for intracerebral hemorrhage: challenges and progress in drug delivery systems. *Neural Regen Res* 2022; 17: 1717–1725.